

OPTICS

Colored and paintable bilayer coatings with high solar-infrared reflectance for efficient cooling

Yijun Chen^{1,2*}, Jyotirmoy Mandal^{1*}, Wenxi Li³, Ajani Smith-Washington⁴, Cheng-Chia Tsai¹, Wenlong Huang¹, Sajan Shrestha¹, Nanfang Yu^{1†}, Ray P. S. Han², Anyuan Cao², Yuan Yang^{1†}

Solar reflective and thermally emissive surfaces offer a sustainable way to cool objects under sunlight. However, white or silvery reflectance of these surfaces does not satisfy the need for color. Here, we present a paintable bilayer coating that simultaneously achieves color and radiative cooling. The bilayer comprises a thin, visible-absorptive layer atop a nonabsorptive, solar-scattering underlayer. The top layer absorbs appropriate visible wavelengths to show specific colors, while the underlayer maximizes the reflection of near-to-short wavelength infrared (NSWIR) light to reduce solar heating. Consequently, the bilayer attains higher NSWIR reflectance (by 0.1 to 0.51) compared with commercial paint monolayers of the same color and stays cooler by as much as 3.0° to 15.6°C under strong sunlight. High NSWIR reflectance of 0.89 is realized in the blue bilayer. The performances show that the bilayer paint design can achieve both color and efficient radiative cooling in a simple, inexpensive, and scalable manner.

INTRODUCTION

Cooling terrestrial objects, such as buildings, vehicles, and data centers, is a critical challenge that we face today. However, cooling is often energy intensive, as predominantly used compression-based coolers consume a substantial amount of electricity. For example, cooling indoor spaces contributes to ~15% of total household electricity usage in the United States (1). Moreover, these cooling designs have a net heating effect and often require ozone-depleting or greenhouse gas-releasing coolants. Hence, alternative approaches with low energy consumption and a net cooling effect are desirable (2, 3).

One such promising alternative is radiative cooling using surfaces with high solar reflectance (R_{solar}) and high emittance (ϵ) including in the long-wavelength infrared (LWIR) atmospheric transmission window. The high R_{solar} minimizes solar heating, while the high ϵ enables radiative heat loss to the cold outer space, allowing the object to stay cool even under sunlight. Because of its passive and eco-friendly operation and its net cooling effect (4–7), radiative cooling designs have been widely investigated. Examples of these designs include white paints (8–10), porous (11) or metallized (12–14) polymers, polymer-dielectric composites (14–18), photonic architectures (19–22), and natural materials (23–25). Usually, these designs maximize radiative cooling by using metal mirrors or white materials with high R_{solar} . However, their broadband reflectance in visible wavelengths restricts their use in real-life situations. For instance, white colors are often not desirable as coatings on buildings or other objects for aesthetic or functional reasons (26–28). Furthermore, the white or silvery glare from these designs can harm human eyes. Colored radiative coolers (CRCs) have been explored to address this issue (29–34). In a CRC, part(s) of the visible spectrum (VIS; 0.4 to 0.74 μm) is selectively absorbed to exhibit the desired color, while other solar wavelengths, in

particular, the near-to-short wavelength infrared (NSWIR; 0.74 to 2.5 μm), are reflected (Fig. 1A). Since NSWIR wavelengths carry 51% of total solar energy, a high NSWIR reflectance (R_{NSWIR}) considerably reduces solar heating. In addition, the cooler also has a high, broadband ϵ to effectively radiate heat to the cold sky. However, existing CRCs are limited in either their performance or their scope. For instance, multilayer photonic CRCs (29, 30) have a high cooling performance but currently are rather expensive and difficult to apply on buildings or cars, which have various shapes, sizes, and textures (35, 36). Colored paints containing TiO_2 and colorants (31, 34), on the other hand, are scalable but usually absorb NSWIR wavelengths to become hot under sunlight. Therefore, simultaneously achieving color and a cooling performance in a highly scalable manner remains a challenge.

Here, we report a bilayer CRC paint coating (Fig. 1, B and C) that consists of a top layer containing a colorant, and an underlayer made of porous poly(vinylidene fluoride-co-hexafluoropropene) [P(VdF-HFP)] or TiO_2 /polymer composite paint. The top layer selectively absorbs visible wavelengths complementary to the desired color but not others, while the underlayer maximizes the backscattering of any sunlight transmitted by the top layer (Fig. 1B). Consequently, the bilayers exhibit near-identical colors and visible reflectances (R_{VIS}) to those of commercial monolayer paint, but a considerably higher R_{NSWIR} , as illustrated in infrared images in Fig. 1D. The increased R_{NSWIR} translates to a higher cooling performance and substantially lower temperatures for the bilayers under sunlight (fig. S1). The performances, especially those of porous P(VdF-HFP)-based bilayers, are considerably better than the control monolayer coatings made using commercial paints. The results are among the best reported so far (29, 30) but were achieved with the simplicity and scalability of paints. For instance, a black porous P(VdF-HFP)-based bilayer that we designed has a nearly identical R_{VIS} (0.07) to that of a monolayer black coating (0.05), but a much higher R_{NSWIR} (0.81 compared with 0.30). Consequently, it can attain a 15.6°C cooler temperature under a mid-day summertime solar intensity of $\sim 1025 \text{ W m}^{-2}$. Note that the cooling achieved by the bilayer designs is not relative to the ambient air as targeted by white or silvered radiative coolers but to commercial paint coatings of the same color.

¹Department of Applied Physics and Applied Mathematics, Columbia University, New York, NY 10027, USA. ²Department of Materials Science and Engineering, College of Engineering, Peking University, Beijing 100871, China. ³Department of Mechanical Engineering, Columbia University, New York, NY 10027, USA. ⁴Department of Physics and Astronomy, College of Arts and Sciences, Howard University, Washington, DC 20059, USA.

*These authors contributed equally to this work.

†Corresponding author. Email: yy2664@columbia.edu (Y.Y.); ny2214@columbia.edu (N.Y.)

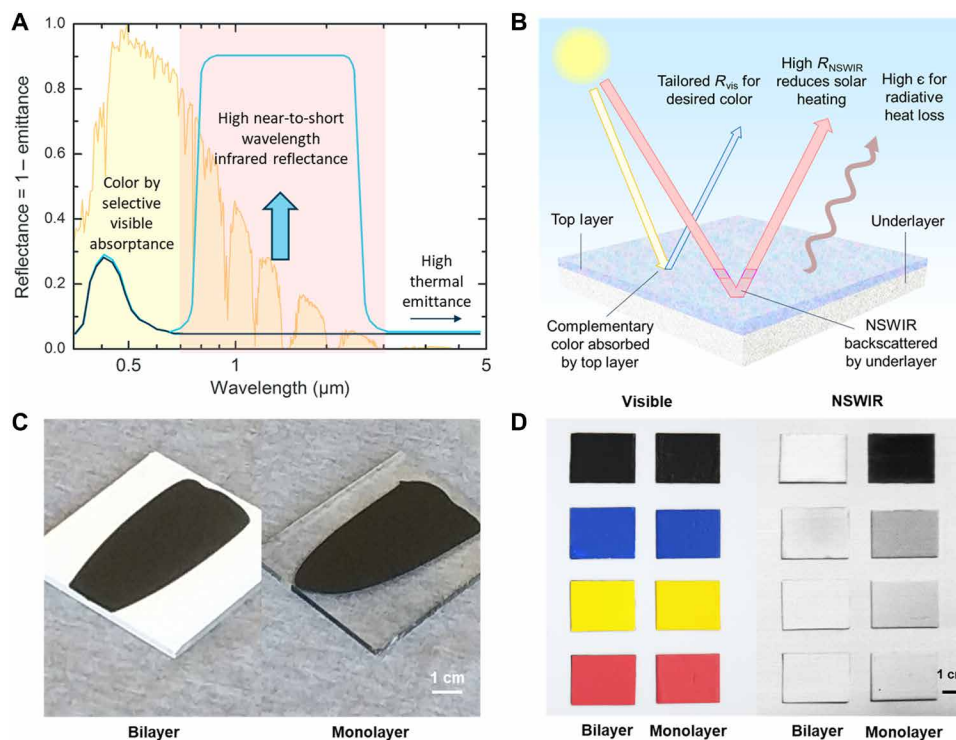


Fig. 1. Bilayer CRCs for enhanced NSWIR reflectance. (A) Enhancing reflectance in the NSWIR, while maintaining the visible reflectance spectrum, can minimize solar absorption for efficient radiative cooling in colored coatings. (B) Schematic illustrating the interaction between sunlight and thermal radiation with the paintable bilayer design. A selective reflection in the visible spectrum yields color, while a high R_{NSWIR} reduces solar heating, and high thermal emittance, including in the LWIR window, maximizes radiative cooling. (C) Photographs showing a bilayer (left) and monolayer (right) painted on plastic substrates. (D) Visible (left) and NSWIR photographs (right) of four differently colored pairs of P(VdF-HFP) bilayer and monolayer coatings. In visible wavelengths, their colors are almost identical, but in the NSWIR, the bilayers are substantially more reflective (whiter). Photo credits: (C) J.M., Columbia University; (D) S.S., Columbia University.

RESULTS

Principle of the bilayer design

To simultaneously achieve color and cooling performance, a surface should maximize its R_{NSWIR} to minimize solar heating and have a high, broadband thermal emittance ϵ required for efficient heat loss to the sky. Commercial colored paint coatings already fulfill the emittance requirement—since solar absorption of colored coatings usually results in above-ambient temperatures, their high broadband emittance (37) (fig. S2) is better suited for cooling than selective LWIR emittance (6, 18). However, their solar reflectance remains less than ideal. In existing monolayer paint designed for cooling, pigments or dyes are used to absorb visible light complementary to the target color, and TiO_2 particles scatter and reflect other visible and NSWIR light because of the difference in refractive indices between TiO_2 and the paint matrix (e.g., polymers). Since NSWIR light, with its longer wavelengths, has a considerably larger penetration depth than visible light (fig. S3), the paint needs to be thick to effectively reflect NSWIR, much thicker than that required for reflecting visible light. However, this leads to an issue that increases the absorption of NSWIR light as follows. Since colorants (dyes or pigments) typically have at least a trailing NSWIR absorptivity (Fig. 2C), the scattering of NSWIR lights across the entire thickness of the monolayer paint substantially lengthens their optical path and results in an increased absorption in NSWIR. Finite-difference time-domain (FDTD) simulations show that when dispersed within a scattering medium (dyed monolayer in Fig. 2D), these colorants can still strongly absorb NSWIR wavelengths because

of long optical paths of scattered light, lowering R_{NSWIR} (Fig. 2A and the monolayer curve in Fig. 2E).

The bilayer design in Fig. 2B, with a thin colored layer atop a thick solar-scattering and nonabsorptive underlayer, can address this problem. Since the top layer is thin (Fig. 2D) and scattering of NSWIR light by the colorant is weak (if the colorants are nanoparticle pigments $\lesssim 50$ nm) or negligible (if they are dissolved dyes), light in the NSWIR wavelengths are transmitted, along short optical paths and without substantial absorption, into the underlayer. Once in the solar-scattering and nonabsorptive underlayer, the NSWIR light is strongly backscattered into the top layer, through which they pass, mostly unimpeded, back into free space, resulting in a high R_{NSWIR} . Furthermore, the thin top layer has the same concentration of colorant and composition as the conventional monolayer with the target color. Although much thinner than the monolayer coating, it still has enough thickness to ensure a strong absorption of visible wavelengths complementary to the target color, while other wavelengths are reflected by either itself or the solar-scattering underlayer. This ensures that the bilayer appears almost identically colored as the monolayer while attaining a higher solar-infrared reflectance.

The bilayer concept is validated by FDTD reflectance simulations of bilayer (5- μm colored top layer + 145- μm porous polymer underlayer) and monolayer (150- μm colored porous layer) coatings (Fig. 2D). The colored layer contains a selective black dye in polymer. The complex refractive index of the dyed polymer is shown in Fig. 2C. As simulated, the bilayer design achieves a near-identical R_{VIS} and, thus,

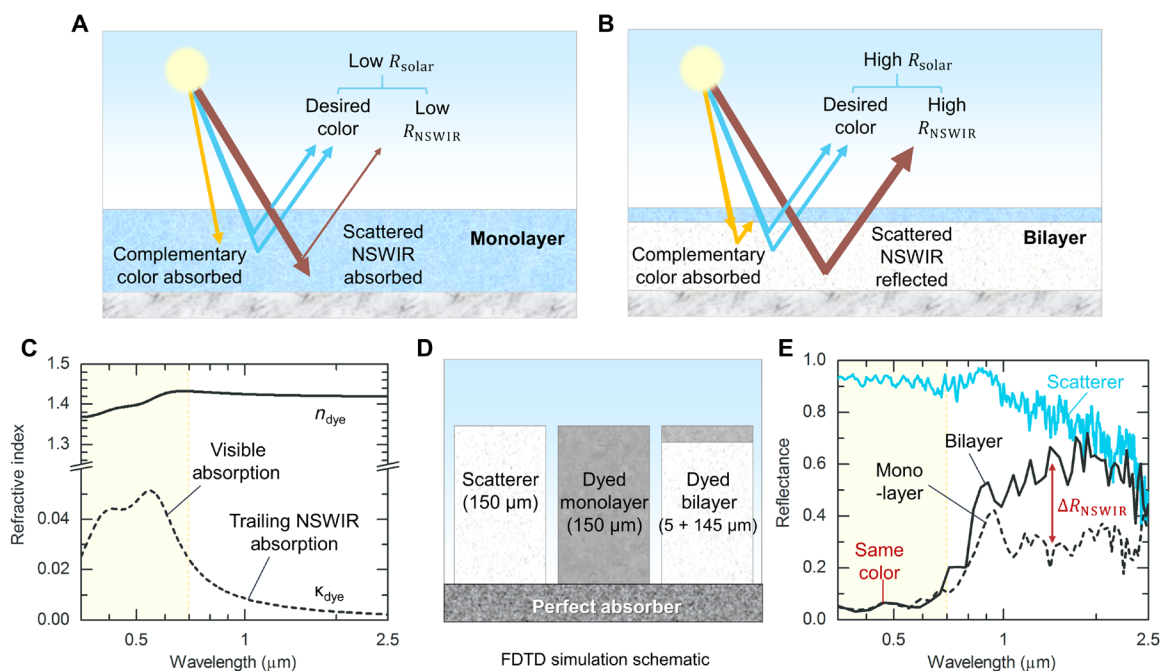


Fig. 2. Principle of the bilayer design. (A and B) Schematic showing the interaction of sunlight with monolayer (A) and bilayer (B) coatings, respectively, and how the latter achieves a higher reflectance. (C) Complex spectral refractive index ($n + ik$) for a polymer containing a selective black dye, showing strong absorption in the visible wavelengths and trailing absorption in the NSWIR wavelengths. (D) Schematic showing the three simulated setups: (left) a solar-scattering porous polymer, (middle) a monolayer of dyed porous polymer with the refractive index in (C), and (right) a bilayer containing the scattering medium at the bottom and a thin film of the monolayer at the top. (E) Simulated reflectances of the three structures in (D).

color as the monolayer. However, its R_{NSWIR} (0.48) is considerably higher than the monolayer's (0.29), leading to a large reduction in solar heating (Fig. 2E). The overall effect is enhanced cooling and same color as the monolayer, with lowered colorant usage.

Comparison with commercial paint monolayers

In this report, we compare the bilayer design concept with monolayer commercial paints of the same colors, which were both fabricated by a simple painting method (fig. S4). Specifically, we investigate two types of solar-scattering underlayers. One is 500- μm -thick layers of $\sim 50\%$ porous P(VdF-HFP), which contains interconnected micro- and nanopores (Fig. 3A), leading to highly efficient backscattering of sunlight. The other is 250- μm nonporous TiO_2 -based white paint coating, which is the commercial radiative cooling standard. The solid volume per area in the two samples are the same. To ensure a fair comparison (i.e., near-indistinguishable visible appearance), the same thickness of commercial colored paints (55/16/40/40 μm for black/blue/red/yellow) is applied as top layers on the P(VdF-HFP) and TiO_2 underlayers. The bilayers are then compared against monolayers made from the same commercial paints, which, being TiO_2 based themselves, are made to have the same thickness as the TiO_2 -based bilayer.

When compared with commercial monolayer paints, the two bilayer designs show near-identical colors but substantially higher values of R_{NSWIR} . As shown in Fig. 3 (C to F), the visible spectra for the mono- and bilayers of each color are closely matched, leading to similar CIE x and y chromaticity values and small lightness differences (Fig. 3B, fig. S5, and table S1). In the NSWIR, however, the reflectances are substantially higher for the porous P(VdF-HFP)-based bilayers, followed by that of the TiO_2 -based bilayers. Specifically, R_{NSWIR} in-

creases from 0.43/0.74/0.69/0.30 in black/blue/red/yellow commercial monolayers to 0.58/0.79/0.80/0.73 for TiO_2 - and 0.63/0.84/0.86/0.81 for porous P(VdF-HFP)-based bilayer coatings, respectively (Table 1). These large enhancements are consistent with the theory stated in the previous section and simulation results. The difference between the porous P(VdF-HFP)- and TiO_2 -based bilayers, meanwhile, is mainly due to the superior NSWIR scattering by the large micropores of P(VdF-HFP) compared with those by small TiO_2 pigments, as demonstrated in our earlier work (11). Porous P(VdF-HFP), therefore, is a good choice as the underlayer. We also tested the specularly of the porous P(VdF-HFP)-based bilayer coatings (figs. S6 to S9). The results indicate that reflections from the coatings are highly diffused. This and the lower R_{VIS} relative to silvery or white coatings show that the colored bilayer design could help address glare issues.

In addition to the high R_{NSWIR} , the bilayer designs also have high thermal emittances (Table 1 and fig. S10) due to the intrinsically emissive nature of the polymers in the top layer and underlayer. The emittance of the underlayers, colored top layers, and bilayers are presented in fig. S11 and table S2, showing that the colored top layers, which are partially transparent but otherwise emissive, and the underlayers, which are highly emissive, collectively exhibit similar emittances to commercial paints (as exemplified by the TiO_2 underlayer). This, along with the high R_{NSWIR} , makes the bilayer a superior cooling design relative to monolayer paint coatings.

The enhancements in R_{NSWIR} achieved through the bilayer approach lead to better daytime cooling performances. We demonstrate this by exposing the bilayer and monolayer samples in Fig. 3 (C to F) to direct sunlight (Fig. 4, A and B). To test the cooling performance in a controlled and consistent environment with similar air convection coefficients, we used solar and infrared transparent 25- μm -thick

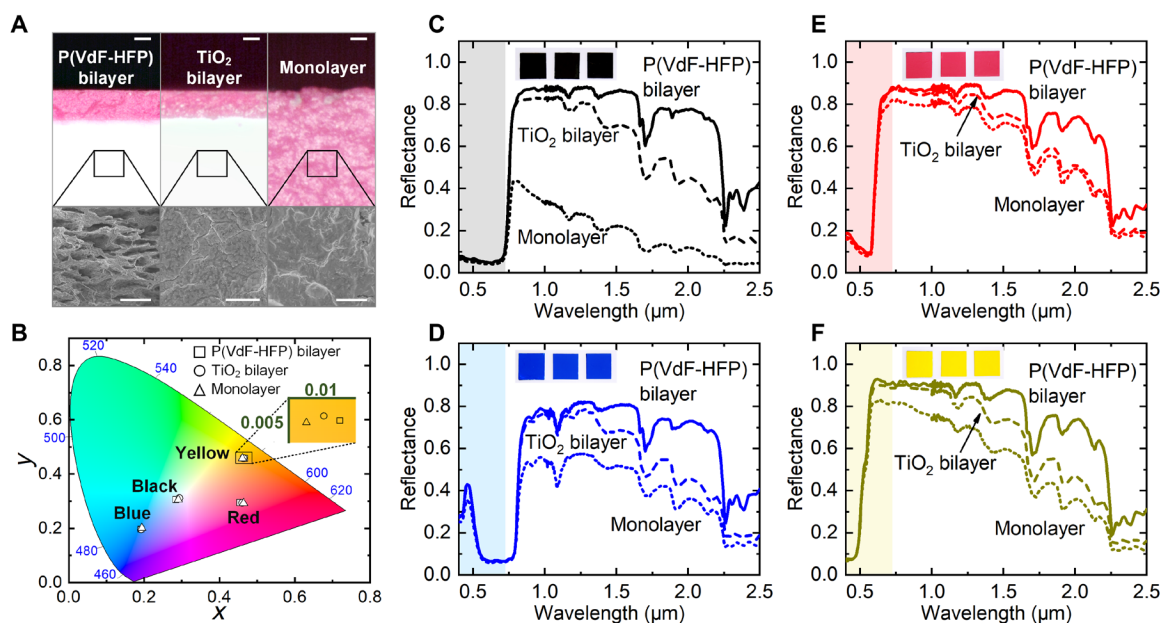


Fig. 3. Structural and optical characterizations of bilayer colored cooling paints. (A) Optical microscopy (top) (scale bars, 20 μm) and scanning electron microscopy (bottom) (scale bars, 5 μm) images of red porous P(VdF-HFP) bilayer, TiO_2 bilayer, and monolayer coatings. (B) The chromaticity of the black, blue, red, and yellow cooling paints shown in the CIE 1931 color space; the inset shows the enlarged view of the chromaticity values of the yellow coatings, indicating a near-identical color. Detailed chromaticity values of the black, blue, red, and yellow coatings are shown in fig. S5. (C to F) The reflectance spectrum of black (C), blue (D), red (E), and yellow (F) cooling paints, respectively. Inset photos in (C) to (F) show from left to right porous P(VdF-HFP)-based bilayer, TiO_2 -based bilayer, and monolayer paints, showing near-identical colors. Photo credit: (A) C.-C.T., Columbia University.

Table 1. The reflectance values of the colored coatings in visible (0.4 to 0.74 μm ; R_{VIS}) and NSWIR wavelengths (0.74 to 2.5 μm ; R_{NSWIR}), and the broadband solar reflectance (0.4 to 2.5 μm ; R_{solar}) and absorptance (0.4 to 2.5 μm ; A_{solar}), as well as the broadband emittance (ϵ across 5- to 15- μm wavelengths). P, T, and M correspond to the porous P(VdF-HFP)-based bilayer, TiO_2 -based bilayer, and monolayer, respectively. Since the emittance is nearly constant across the 5- to 15- μm wavelengths, the selective LWIR emittance is nearly identical to the broadband emittance, as shown in table S3.

Sample	Black			Blue			Red			Yellow		
	P	T	M	P	T	M	P	T	M	P	T	M
R_{VIS}	0.07	0.06	0.05	0.17	0.17	0.15	0.39	0.38	0.35	0.59	0.58	0.54
R_{NSWIR}	0.81	0.73	0.30	0.63	0.58	0.43	0.84	0.79	0.74	0.86	0.80	0.69
$R_{\text{solar}} = 1 - A_{\text{solar}}$	0.44	0.39	0.17	0.40	0.37	0.29	0.61	0.58	0.54	0.72	0.69	0.61
ϵ	0.95	0.95	0.96	0.95	0.95	0.95	0.95	0.95	0.96	0.95	0.96	0.96

poly(ethylene) (PE) films to shield the setup, as has been done in previous studies (20, 25).

For the extreme case (the black samples), because of the large contrast in R_{NSWIR} [0.81 for porous P(VdF-HFP) bilayer, 0.73 for TiO_2 bilayer, and 0.30 for monolayer; Table 1], the porous P(VdF-HFP)- and TiO_2 -based bilayers remain 15.6°C and 13.2°C cooler than the monolayer under $\sim 1025 \text{ W m}^{-2}$ solar irradiation (Fig. 4C). For blue/red/yellow colors, on the other hand, the porous P(VdF-HFP)- and TiO_2 -based bilayers remain 6.6°C/3.0°C/7.3°C and 4.3°C/1.8°C/5.2°C cooler than the monolayer commercial paints (Fig. 4, D to F), respectively. These large temperature differences are consistent with theoretical simulations (fig. S12), assuming a convective heat transfer coefficient (h_c) of ~ 5 to $7 \text{ W m}^{-2} \text{ K}^{-1}$ observed in the literature (20, 36). We also conducted tests without PE convection shields. Even with larger convective effects, the black/blue/red/yellow bilayers were still 6.4°C/3.4°C/2.6°C/4.5°C [porous P(VdF-HFP)] and 4.6°C/1.9°C/1.5°C/

3.8°C (TiO_2) cooler than the monolayer coatings (fig. S13), indicating their performance under breezy conditions. In certain situations, where the solar intensities are sufficiently low, light-yellow bilayers with high solar reflectances achieved subambient cooling (fig. S14). These results demonstrate that the bilayer design, especially based on porous P(VdF-HFP), is attractive for reducing temperatures and air-conditioning costs in buildings, cars, and other terrestrial objects. From a practical perspective, the performances are achieved with a simple painting process while satisfying the aesthetic requirement for color.

DISCUSSION

Pushing the bilayer performance

While the above demonstration shows the superior optical and thermal performance of the bilayers over monolayers, commercial paints are not necessarily ideal as top layers, as they usually contain

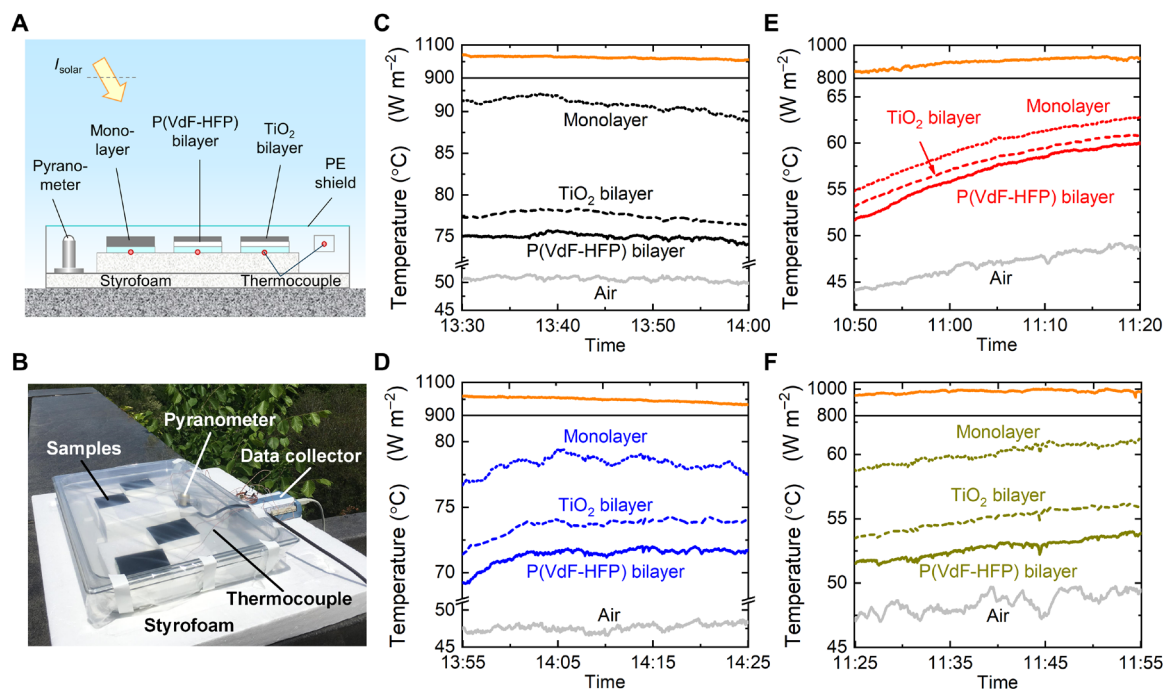


Fig. 4. Outdoor temperature tests of the colored cooling paints. (A and B) Schematic and photograph of the setup for the temperature tests under sunlight. (C to F) Detailed solar intensity (top part of the y axis) and temperature (lower part of the y axis) data in the outdoor tests of the black (C), blue (D), red (E), and yellow (F) cooling paints, respectively. As evident, for all colors, the P(VdF-HFP)-based bilayers are the coolest, closely followed by the TiO₂-based bilayers. Both bilayers are substantially cooler than the monolayers. Photo credit: (B) Y.C., Columbia University.

colorants that are NSWIR absorptive and, often, pigments that scatter and absorb NSWIR wavelengths. The ideal top layer should exhibit highly selective visible absorption where required and minimal scattering of NSWIR wavelengths. The highly selective visible absorption has been widely studied, including dielectric film-coated metal flakes as pigments by Smith *et al.* (32, 33) and a comprehensive investigation of pigments by Levinson *et al.* (38, 39); minimal NSWIR scattering can be achieved by using small pigments (with sizes <100 nm) or organic dyes dissolved in polymers. Figure 5A shows an illustration of this concept where the colorant is a highly selective blue dye (Sudan Blue II) dispersed in solid P(VdF-HFP) and the underlayer is a porous P(VdF-HFP) film, which has a high R_{NSWIR} of 0.89. This performance is also much higher than the bilayer with commercial blue top layer (R_{NSWIR} of 0.63). If R_{VIS} are the same in the two coatings, the large R_{NSWIR} could reduce noon-time ($I_{\text{solar}} = 1000 \text{ W m}^{-2}$) surface temperatures by 12°C under still air ($h_c = 5 \text{ W m}^{-2} \text{ K}^{-1}$) or 6°C under mild winds ($h_c = 15 \text{ W m}^{-2} \text{ K}^{-1}$) (fig. S1). The results indicate that optimizing the colored top layer can further enhance the cooling performance of the bilayer design.

Besides achieving different hues through the choice of colorant, the bilayer design can also achieve different lightnesses or shades for the same hue. As demonstrated in Fig. 5B, for bilayers with Sudan Blue colorant, a thin top layer can yield a whitish blue color, while thicker top layers show a deeper blue. By mixing with Perylene Black, darker blue-black shades can be achieved. R_{NSWIR} , however, remains appealingly high regardless of the shade (0.86, 0.80, and 0.73 for three curves in Fig. 5B). In applications where the reduction in glare while maintaining hue is important, this can be highly useful. The concept of the bilayer is one that can be generalized to any dye, pigment,

polymer, or other paint components to achieve specific attributes. For instance, the pigments in the top layer and the polymer in the underlayer can be chosen to achieve high stability. We demonstrated this by placing porous P(VdF-HFP)-based bilayers outdoors or in an oven at 60°C for 30 days, during which the reflectance and emittance of the coatings showed no appreciable changes (~0.01 or less; fig. S15). We note that issues such as potential nighttime condensation of water on the coatings due to greater cooling performance can be similarly addressed by using hydrophobic, weather-resistant top layers. Furthermore, the bilayer design can also yield different surface finishes by use of suitable polymer binders in the top layer (Fig. 5C), which is difficult for photonic designs. This is important, for instance, to the automotive industry. We also note that all these attributes can potentially be extended to textiles, on which photonic designs may be difficult to implement. By dipping white fibers into dye suspensions, core-shell colored fibers with high solar reflectance may be created (Fig. 5D). Collectively, these attributes underscore the versatility of the bilayer design and its potential significance to coatings industries.

A last point, in relation to the paintability of the bilayer design, is the sensitivity of its optical performance to fabrication parameters. To test for this, we conducted a sensitivity analysis, investigating factors such as replicability of the optical performances over repeated fabrications following the same procedure, changing the composition of the precursor for the P(VdF-HFP) underlayer, and testing the effect of altering the thickness of the top layer. Our results, presented in figs. S16 to S18, show that the optical performances of the coatings are highly replicable for a given fabrication procedure and that the use of different compositions of precursors to fabricate the P(VdF-HFP) underlayer and varying the thickness of the top layer have minimal impact on R_{NSWIR} and thermal emittance. All the three tests indicate

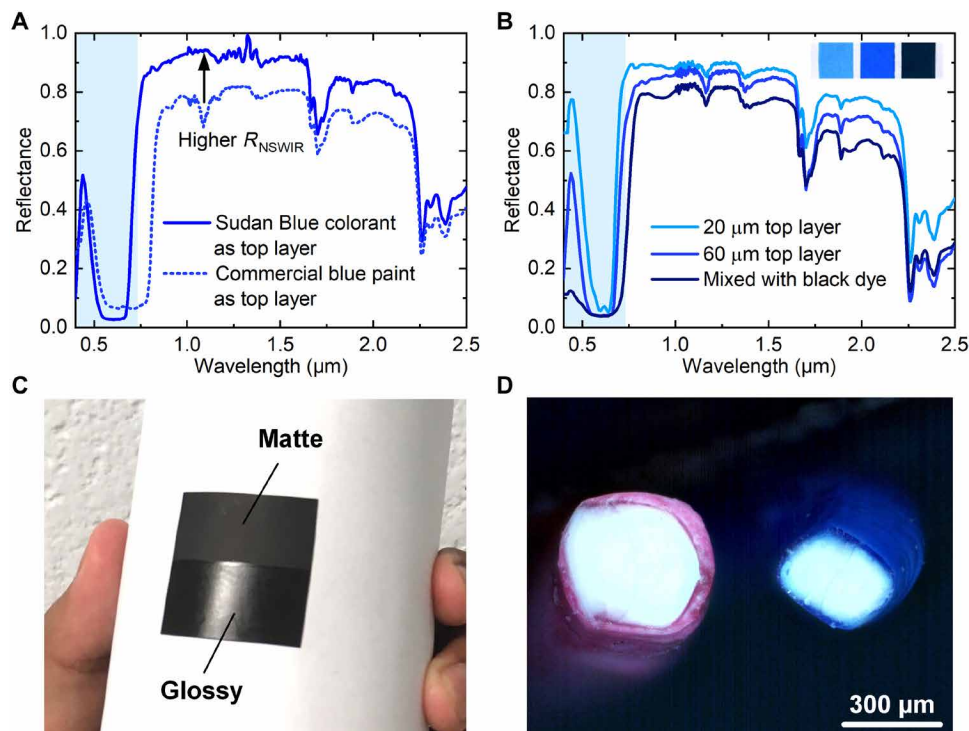


Fig. 5. Tuning colored top layer in the bilayer cooling paints. (A) Using more selective dye as colorant to further improve the solar-infrared reflectance of the bilayer sample. (B) Changing the top-layer thickness and mixing Sudan Blue dye with Perylene Black dye to change the color shade of the bilayer cooling paints. The inset photo shows that the color gets darker after increasing the colored layer thickness from 20 μm (left) to 60 μm (middle) and adding Perylene Black (right). (C) By using poly(methyl methacrylate) (PMMA) binder in the top layer, a glossy sheen can be achieved, while with P(VdF-HFP) binder, a matte texture is achieved. (D) The bilayer concept can also be extended to fibers, which could lead to its potential uses in textiles. Photo credits: (C) J.M., Columbia University; (D) C.-C.T., Columbia University.

the robustness of the fabrication procedure at yielding high cooling performance.

In conclusion, we propose a simple, inexpensive, and scalable method to make a paintable bilayer colored radiative cooling coating, which comprises a top layer to absorb complementary visible wavelengths to the desired colors, and an underlayer to strongly reflect sunlight in NSWIR wavelengths. Theoretical simulations and optical characterizations reveal that the bilayer design can reduce solar-infrared absorption by the colorants and thereby achieve a higher R_{NSWIR} than its monolayer counterpart. When compared with conventional colored monolayer paint with the same color, the R_{NSWIR} is improved by up to 0.51 by using porous P(VdF-HFP) as a solar-scattering underlayer. As a result, high cooling performances are achieved, e.g., for the black porous P(VdF-HFP)-based bilayer, a 15.6°C lower temperature than that of the monolayer black coating was attained under a solar intensity $\sim 1025 \text{ W m}^{-2}$. By changing the dye components and their amounts, we can further increase R_{NSWIR} (e.g., to 0.89 for blue) and change color shades of the bilayer paints. The paintable bilayer designs, which substantially outperform commercial monolayer paints, demonstrate a practical and efficient solution to cooling colored objects in a green and energy-saving manner.

MATERIALS AND METHODS

Fabrication of colored cooling paint coatings

The bilayer colored cooler was fabricated via a two-step process (fig. S4): Porous P(VdF-HFP)- or TiO_2 -based white underlayer was first painted

on a substrate, and then, a layer containing a colorant was painted on top. The porous P(VdF-HFP) underlayer was created using a previously outlined phase inversion method (11): A solution of P(VdF-HFP) powder (Kynar Flex 2801)/acetone/water with a weight ratio of 1:8:1 was painted on a plastic substrate to form a white layer with a thickness of $\sim 500 \mu\text{m}$. The TiO_2 -based commercial white paint (Sherwin-Williams, 636613 High Reflective White) was painted onto a substrate to form a $\sim 250\text{-}\mu\text{m}$ -thick layer. To make the blue, red, and yellow top layers shown in Figs. 1 to 4, commercial paints (2066-30 Big Country Blue, 2086-30 Rosy Blush, and 2021-30 Sunshine from Benjamin Moore, respectively) were used. For black top layers, Perylene Black (Oakwood Chemical) as the colorant (1 mg ml^{-1}) and P(VdF-HFP) as the polymer matrix (150 mg ml^{-1}) are dispersed in acetone to make the paint. The blue top layers shown in Fig. 5 were made in the same way as black, except that Sudan Blue II dye (Sigma-Aldrich) was used as the colorant. The monolayer samples were obtained by coating the same colored paints in the bilayer designs onto poly(methyl methacrylate) (PMMA) substrates, with thicknesses equal to those of the corresponding TiO_2 -based bilayers.

Optical characterization

The visible and NSWIR photographs of the samples were taken using Nikon D3300 camera and NIRvana ST 640 camera, respectively. Microscopy was performed using the Zeiss Axio Imager.A2m optical microscope and Zeiss Sigma VP scanning electron microscope. The reflectance spectra were taken separately in two wavelength ranges: visible to near-infrared (0.4 to 1.0 μm) and near-infrared to LWIR

(1.0 to 15 μm) for incident angles of 30°. In the first range, the reflectance was measured using an integrating sphere (model IS200, Thorlabs) containing a silicon detector and coupled to a high-power supercontinuum laser (SuperK EXTREME, NKT Photonics) and a tunable filter (Fianium LLTF contrast). The sample was put inside the integrating sphere. A calibrated diffuse reflector (item SM05CP2C, Thorlabs) was used as the reference. In the second range, reflectance was measured using a gold integrating sphere (model 4P-GPS-020-SL, Labsphere) coupled with a mercury cadmium telluride detector and a Fourier transform infrared spectrometer (VERTEX 70v, Bruker). A gold-coated aluminum foil was used as the reference. The spectra in the two ranges were then patched to obtain the final reflectance. The transmission spectra were obtained in the same way, except that the sample was placed at the mouth of the integrating sphere.

Outdoor temperature measurements

The thermal tests were conducted using the setup (Fig. 4B) in New York on 23, 26, 27, and 28 June 2019 for blue, black, yellow, and red samples, respectively. For each color, porous P(VdF-HFP)-based bilayer, TiO₂-based bilayer, and monolayer samples with an area of 7.5 cm by 7.5 cm were placed in a transparent open-top polycarbonate box. A low-density PE film was tautly drawn above the samples as a wind shield to reduce the convective heat transfer without substantially hindering solar and thermal infrared transmission. All samples were supported by styrofoam, and the box itself was placed on another large white styrofoam to reduce the heat transfer between the samples and ground. The temperature of each sample was measured by a thermocouple pressed to its back face by a black tape, which also served as a solar absorptive layer. A thermocouple shielded from sunlight was used to measure air temperature in the box. A pyranometer (Apogee, SP-510) connected to the computer was placed beside the sample to measure the total (direct + diffuse) solar intensity.

Reflectance and emittance calculation

The reflectance \bar{R} is defined as the ratio of the reflected solar intensity within a certain wavelength range (λ_1 to λ_2) to the total incident solar intensity in the same range, as expressed below

$$\bar{R} = \frac{\int_{\lambda_1}^{\lambda_2} I_{\text{solar}}(\lambda) R(\lambda) d\lambda}{\int_{\lambda_1}^{\lambda_2} I_{\text{solar}}(\lambda) d\lambda} \quad (1)$$

where $I_{\text{solar}}(\lambda)$ is the ASTM G173-03 global solar intensity spectrum, and $R(\lambda)$ is the sample's spectral reflectance. Ranges 0.4 to 0.74 μm and 0.74 to 2.5 μm correspond to the wavelength range used in the calculation of reflectance in the visible and NSWIR wavelengths, respectively.

Similarly, the thermal emittance $\bar{\epsilon}$ is defined as the ratio of the spectral intensity within a certain wavelength area (λ_1 to λ_2) to that of a standard blackbody at the same temperature and wavelength same area, as expressed below

$$\bar{\epsilon} = \frac{\int_{\lambda_1}^{\lambda_2} I_{\text{bb}}(T, \lambda) \epsilon(T, \lambda) d\lambda}{\int_{\lambda_1}^{\lambda_2} I_{\text{bb}}(T, \lambda) d\lambda} \quad (2)$$

where $I_{\text{bb}}(T, \lambda)$ is the spectral intensity emitted by a standard blackbody with a temperature of T , and $\epsilon(T, \lambda)$ is the sample's spectral emittance.

Calculating color from the spectrum

Tristimulus values X , Y , and Z are calculated to measure the response of human eyes to the light based on the CIE color-matching functions (40) $\bar{x}(\lambda)$, $\bar{y}(\lambda)$, and $\bar{z}(\lambda)$ and the sample's reflectance spectrum $R(\lambda)$ using the formulas below

$$X = 100 \frac{\int I(\lambda) R(\lambda) \bar{x}(\lambda) d\lambda}{\int I(\lambda) \bar{y}(\lambda) d\lambda} \quad (3)$$

$$Y = 100 \frac{\int I(\lambda) R(\lambda) \bar{y}(\lambda) d\lambda}{\int I(\lambda) \bar{y}(\lambda) d\lambda} \quad (4)$$

$$Z = 100 \frac{\int I(\lambda) R(\lambda) \bar{z}(\lambda) d\lambda}{\int I(\lambda) \bar{y}(\lambda) d\lambda} \quad (5)$$

Here, CIE Illuminant D65 spectrum $I(\lambda)$ is used to portray the standard open-air illumination conditions. The chromaticity is then specified by the two normalized values (x and y) derived from the tristimulus values and located in the CIE 1931 color space

$$x = \frac{X}{X + Y + Z} \quad (6)$$

$$y = \frac{Y}{X + Y + Z} \quad (7)$$

The lightness (L) of the color is calculated by the Lab-XYZ color space conversion (40)

$$L = 116f\left(\frac{Y}{Y_n}\right) - 16 \quad (8)$$

where $Y_n = 100$, corresponding to the CIE XYZ tristimulus value of the reference white point under Illuminant D65 and

$$f(t) = \begin{cases} t^{1/3} & \text{if } t > \left(\frac{6}{29}\right)^3 \\ \frac{t}{3 \times \left(\frac{6}{29}\right)^2} + \frac{4}{29} & \text{if } t < \left(\frac{6}{29}\right)^3 \end{cases} \quad (9)$$

FDTD simulation

FDTD simulations of the structures shown in Fig. 2D were carried out using FDTD Solutions 8.6.1 software by Lumerical. For the scattering medium, a polymer ($n \sim 1.39$) (11) with light scattering air voids ($n \sim 1$) of sizes 0.1 to 0.5 μm was used. The thickness was chosen to be 150 μm . For the dyed monolayer, a 150- μm -thick, optically homogeneous, nonscattering polymer-dye mixture with the complex refractive index shown in Fig. 2C, and containing light scattering air voids with the same size distribution as the scattering medium, was used instead. The refractive index was generated using a simple Lorentz oscillator model. The bilayer consisted of 5 μm of the dyed monolayer placed atop of a 145- μm solar scattering layer. A plane wave light source was used, and the spectrally resolved backscattered power and, thus, reflectance were measured by a monitor placed above the aforementioned structures. As shown in Fig. 2E, the simulated NSWIR reflectance for the bilayer is indeed higher than that of the monolayer and validates our bilayer approach.

SUPPLEMENTARY MATERIALS

Supplementary material for this article is available at <http://advances.sciencemag.org/cgi/content/full/6/17/eaaz5413/DC1>

REFERENCES AND NOTES

- U.S. Energy Information Administration, Annual energy outlook 2019 with projections to 2050; www.eia.gov/outlooks/aeo/pdf/aeo2019.pdf.
- G. B. Smith, C.-G. Granqvist, *Green Nanotechnology—Solutions for Sustainability and Energy in the Built Environment* (CRC Press, 2010).
- M. Santamouris, J. Feng, Recent progress in daytime radiative cooling: Is it the air conditioner of the future? *Buildings* **8**, 168 (2018).
- C. G. Granqvist, A. Hjortsberg, Surfaces for radiative cooling: Silicon monoxide films on aluminum. *Appl. Phys. Lett.* **36**, 139–141 (1980).
- C. G. Granqvist, G. A. Niklasson, Solar energy materials for thermal applications: A primer. *Sol. Energy Mater. Sol. Cells* **180**, 213–226 (2018).
- M. M. Hossain, M. Gu, Radiative cooling: Principles, progress, and potentials. *Adv. Sci.* **3**, 1500360 (2016).
- B. Zhao, M. Hu, X. Ao, N. Chen, G. Pei, Radiative cooling: A review of fundamentals, materials, applications, and prospects. *Appl. Energy* **236**, 489–513 (2019).
- C. S. Wojtyciak, Radiative cooling surface coatings. Patent WO. 2002098996 (2002).
- B. Bhatia, A. Leroy, Y. Shen, L. Zhao, M. Gianello, D. Li, T. Gu, J. Hu, M. Soljačić, E. N. Wang, Passive directional sub-ambient daytime radiative cooling. *Nat. Commun.* **9**, 5001 (2018).
- Cool Roof Rating Council, Rated products directory; <https://coolroofs.org/directory>.
- J. Mandal, Y. Fu, A. C. Overvig, M. Jia, K. Sun, N. N. Shi, H. Zhou, X. Xiao, N. Yu, Y. Yang, Hierarchically porous polymer coatings for highly efficient passive daytime radiative cooling. *Science* **362**, 315–318 (2018).
- A. R. Gentle, G. B. Smith, A subambient open roof surface under the mid-summer sun. *Adv. Sci.* **2**, 1500119 (2015).
- J.-L. Kou, Z. Jurado, Z. Chen, S. H. Fan, A. J. Minnich, Daytime radiative cooling using near-black infrared emitters. *ACS Photonics* **4**, 626–630 (2017).
- N. Yu, J. Mandal, A. Overvig, N. N. Shi, Systems and methods for radiative cooling and heating. Patent WO. 2016205717 (2016).
- A. R. Gentle, G. B. Smith, Radiative heat pumping from the earth using surface phonon resonant nanoparticles. *Nano Lett.* **10**, 373–379 (2010).
- Y. Zhai, Y. Ma, S. N. David, D. Zhao, R. Lou, G. Tan, R. Yang, X. Yin, Scalable-manufactured randomized glass-polymer hybrid metamaterial for daytime radiative cooling. *Science* **355**, 1062–1066 (2017).
- D. Zhao, A. Aili, Y. Zhai, J. Lu, D. Kidd, G. Tan, X. Yin, R. Yang, Subambient cooling of water: Toward real-world applications of daytime radiative cooling. *Joule* **3**, 111–123 (2018).
- A. R. Gentle, G. B. Smith, Optimized infra-red spectral response of surfaces for sub-ambient sky cooling as a function of humidity and operating temperature. *Photon. Sol. Energy Syst. III* **7725**, 772502 (2010).
- E. Rephaeli, A. Raman, S. H. Fan, Ultrabroadband photonic structures to achieve high-performance daytime radiative cooling. *Nano Lett.* **13**, 1457–1461 (2013).
- A. P. Raman, M. A. Anoma, L. Zhu, E. Rephaeli, S. H. Fan, Passive radiative cooling below ambient air temperature under direct sunlight. *Nature* **515**, 540 (2014).
- Z. Chen, L. X. Zhu, A. Raman, S. H. Fan, Radiative cooling to deep sub-freezing temperatures through a 24-h day-night cycle. *Nat. Commun.* **7**, 13729 (2016).
- C. Zou, G. Ren, M. M. Hossain, S. Niranjan, W. Withayachumankul, T. Ahmed, M. Bhaskaran, S. Sriram, M. Gu, C. Fumeaux, Metal-loaded dielectric resonator metasurfaces for radiative cooling. *Adv. Opt. Mater.* **5**, 1700460 (2017).
- S. H. Choi, S.-W. Kim, Z. Ku, M. A. Visbal-Onufrak, S.-R. Kim, K.-H. Choi, H. Ko, W. Choi, A. M. Urbas, T.-W. Goo, Y. L. Kim, Anderson light localization in biological nanostructures of native silk. *Nat. Commun.* **9**, 452 (2018).
- N. N. Shi, C.-C. Tsai, M. J. Carter, J. Mandal, A. C. Overvig, M. Y. Sfeir, M. Lu, C. L. Craig, G. D. Bernard, Y. Yang, N. F. Yu, Nanostructured fibers as a versatile photonic platform: Radiative cooling and waveguiding through transverse anderson localization. *Light Sci. Appl.* **7**, 37 (2018).
- T. Li, Y. Zhai, S. He, W. Gan, Z. Wei, M. Heidarinejad, D. Dalgo, R. Mi, X. Zhao, J. Song, J. Dai, C. Chen, A. Aili, A. Vellore, A. Martini, R. Yang, J. Srebric, X. Yin, L. Hu, A radiative cooling structural material. *Science* **364**, 760–763 (2019).
- L. Cai, Y. Peng, J. Xu, C. Zhou, C. Zhou, P. Wu, D. Lin, S. Fan, Y. Cui, Temperature regulation in colored infrared-transparent polyethylene textiles. *Joule* **3**, 1478–1486 (2019).
- L. M. Lozano, S. Hong, Y. Huang, H. Zandavi, Y. A. El Aoud, Y. Tsurimaki, J. Zhou, Y. Xu, R. M. Osgood, G. Chen, S. V. Boriskina, Optical engineering of polymer materials and composites for simultaneous color and thermal management. *Opt. Mater. Express* **9**, 1990–2005 (2019).
- A. Synnefa, M. Santamouris, K. Apostolakis, On the development, optical properties and thermal performance of cool colored coatings for the urban environment. *Sol. Energy* **81**, 488–497 (2007).
- G. J. Lee, Y. J. Kim, H. M. Kim, Y. J. Yoo, Y. M. Song, Colored Passive Radiative Cooler: Colored, daytime radiative coolers with thin-film resonators for aesthetic purposes (Advanced Optical Materials 22/2018). *Adv. Opt. Mater.* **6**, 1870085 (2018).
- W. Li, Y. Shi, Z. Chen, S. Fan, Photonic thermal management of coloured objects. *Nat. Commun.* **9**, 4240 (2018).
- H. Gonome, M. Nakamura, J. Okajima, S. Maruyama, Artificial chameleon skin that controls spectral radiation: Development of chameleon cool coating (C³). *Sci. Rep.* **8**, 1196 (2018).
- G. B. Smith, A. Gentle, P. Swift, A. Earp, N. Mronga, Coloured paints based on coated flakes of metal as the pigment, for enhanced solar reflectance and cooler interiors: Description and theory. *Sol. Energy Mater. Sol. Cells* **79**, 163–177 (2003).
- G. B. Smith, A. Gentle, P. D. Swift, A. Earp, N. Mronga, Coloured paints based on iron oxide and silicon oxide coated flakes of aluminium as the pigment, for energy efficient paint: Optical and thermal experiments. *Sol. Energy Mater. Sol. Cells* **79**, 179–197 (2003).
- J. Song, J. Qin, J. Qu, Z. Song, W. Zhang, X. Xue, Y. Shi, T. Zhang, W. Ji, R. Zhang, H. Zhang, Z. Zhang, X. Wu, The effects of particle size distribution on the optical properties of titanium dioxide rutile pigments and their applications in cool non-white coatings. *Sol. Energy Mater. Sol. Cells* **130**, 42–50 (2014).
- X. Lu, P. Xu, H. Wang, T. Yang, J. Hou, Cooling potential and applications prospects of passive radiative cooling in buildings: The current state-of-the-art. *Renew. Sustain. Energy Rev.* **65**, 1079–1097 (2016).
- M. Zeyghami, D. Y. Goswami, E. Stefanakos, A review of clear sky radiative cooling developments and applications in renewable power systems and passive building cooling. *Sol. Energy Mater. Sol. Cells* **178**, 115–128 (2018).
- Mikron Instrument Company Inc., Table of emissivity of various surfaces; www-eng.lbl.gov/~dw/projects/DW4229_LHC_detector_analysis/calculations/emissivity2.pdf.
- R. Levinson, P. Berdahl, H. Akbari, Solar spectral optical properties of pigments—Part I: Model for deriving scattering and absorption coefficients from transmittance and reflectance measurements. *Sol. Energy Mater. Sol. Cells* **89**, 319–349 (2005).
- R. Levinson, P. Berdahl, H. Akbari, Solar spectral optical properties of pigments—Part II: Survey of common colorants. *Sol. Energy Mater. Sol. Cells* **89**, 351–389 (2005).
- J. Schanda, *Colorimetry: Understanding the CIE System* (John Wiley & Sons, 2007).
- Arkema, Kynar & Kynar flex PVDF performance characteristics and data (2017); <https://www.extremematerials-arkema.com/en/product-families/kynar-pvdf-family/download-performance-characteristics-data-brochure/>.
- Arkema, New fluoropolymer latex technology for cool materials solutions across an expanded color space (2008); <http://coolcolors.lbl.gov/assets/docs/PAC-2008-03-06/Arkema-slides.pdf>.
- J. Mandal, D. Wang, A. C. Overvig, N. N. Shi, D. Paley, A. Zangiabadi, Q. Cheng, K. Barnak, N. F. Yu, Y. Yang, Scalable, "dip-and-dry" fabrication of a wide-angle plasmonic selective absorber for high-efficiency solar-thermal energy conversion. *Adv. Mater.* **29**, 1702156 (2017).
- H. Karttunen, P. Kröger, H. Oja, M. Poutanen, K. J. Donner, *Fundamental Astronomy* (Springer, 2016).

Acknowledgments

Funding: Y.C. would like to acknowledge the financial support from the China Scholarship Council (no. 201806010292). J.M. acknowledges support from the Schmidt Science Fellows, in partnership with the Rhodes Trust. The optical reflectance measurements were performed on instruments purchased by no. FA9550-16-1-0322 through the Defense University Research Instrumentation Program awarded to N.Y. **Author contributions:** Y.C. and J.M. contributed equally to this work. J.M. conceived the bilayer design based on a realization of the variation of optical penetration depth with wavelength and performed the optical simulations to validate the design. Y.C. fabricated and optimized the samples for cooling performance. Y.C. and J.M. characterized the samples. Y.C. and J.M. performed the thermal tests. Y.Y. supervised the study and designed the experiments. N.Y. provided advice on the optical measurements and provided helpful suggestions for the manuscript. W.L. carried out the COMSOL simulations. C.-C.T. and S.S. assisted with the optical characterizations and imaging. Y.C., J.M., and Y.Y. wrote the manuscript. All authors discussed the results and viewed the manuscript. **Competing interests:** J.M., Y.Y., and Y.C. are inventors on a patent application related to this work (no. US 62/901,932, filed 18 September 2019). The authors declare no other competing interests. **Data and materials availability:** All data needed to evaluate the conclusions in the paper are present in the paper and/or the Supplementary Materials. Additional data related to this paper may be requested from the authors.

Submitted 18 September 2019

Accepted 31 January 2020

Published 24 April 2020

10.1126/sciadv.aaz5413

Citation: Y. Chen, J. Mandal, W. Li, A. Smith-Washington, C.-C. Tsai, W. Huang, S. Shrestha, N. Yu, R. P. S. Han, A. Cao, Y. Yang, Colored and paintable bilayer coatings with high solar-infrared reflectance for efficient cooling. *Sci. Adv.* **6**, eaaz5413 (2020).

Colored and paintable bilayer coatings with high solar-infrared reflectance for efficient cooling

Yijun Chen, Jyotirmoy Mandal, Wenxi Li, Ajani Smith-Washington, Cheng-Chia Tsai, Wenlong Huang, Sajan Shrestha, Nanfang Yu, Ray P. S. Han, Anyuan Cao and Yuan Yang

Sci Adv 6 (17), eaaz5413.
DOI: 10.1126/sciadv.aaz5413

ARTICLE TOOLS	http://advances.sciencemag.org/content/6/17/eaaz5413
SUPPLEMENTARY MATERIALS	http://advances.sciencemag.org/content/suppl/2020/04/20/6.17.eaaz5413.DC1
REFERENCES	This article cites 34 articles, 3 of which you can access for free http://advances.sciencemag.org/content/6/17/eaaz5413#BIBL
PERMISSIONS	http://www.sciencemag.org/help/reprints-and-permissions

Use of this article is subject to the [Terms of Service](#)

Science Advances (ISSN 2375-2548) is published by the American Association for the Advancement of Science, 1200 New York Avenue NW, Washington, DC 20005. The title *Science Advances* is a registered trademark of AAAS.

Copyright © 2020 The Authors, some rights reserved; exclusive licensee American Association for the Advancement of Science. No claim to original U.S. Government Works. Distributed under a Creative Commons Attribution NonCommercial License 4.0 (CC BY-NC).